Contents lists available at ScienceDirect

Nuclear Inst. and Methods in Physics Research, A

journal homepage: www.elsevier.com/locate/nima

A new cylindrical photon-veto detector for the $K_L \to \pi^0 \nu \bar{\nu}$ experiment

R. Murayama [a,1,*], M. Togawa [a,1], J.K. Ahn [b], J. Comfort [c], T. Inagaki [d], M. Isoe [a], I. Kamiji [e],
E.J. Kim [f], J.L. Kim [b,2], T.K. Komatsubara [d,g], G.Y. Lim [d,g], T. Matsumura [h], K. Miyazaki [a],
H. Nanjo [e,3], T. Nomura [d,g], H. Okuno [d], E. Pod [i], T. Sato [d], K. Shiomi [d,g], Y. Tajima [j], T. Toyoda [a],
Y.W. Wah [i], H. Watanabe [d,g], T. Yamanaka [a]

[a] *Department of Physics, Osaka University, Toyonaka, Osaka 560-0043, Japan*
[b] *Department of Physics, Korea University, Seoul 02841, Republic of Korea*
[c] *Department of Physics, Arizona State University, Tempe, AZ 85287, USA*
[d] *Institute of Particle and Nuclear Studies, High Energy Accelerator Research Organization (KEK), Tsukuba, Ibaraki 305-0801, Japan*
[e] *Department of Physics, Kyoto University, Kyoto 606-8502, Japan*
[f] *Division of Science Education, Jeonbuk National University, Jeonju 54896, Republic of Korea*
[g] *J-PARC Center, Tokai, Ibaraki 319-1195, Japan*
[h] *Department of Applied Physics, National Defense Academy, Kanagawa 239-8686, Japan*
[i] *Enrico Fermi Institute, University of Chicago, Chicago, IL 60637, USA*
[j] *Department of Physics, Yamagata University, Yamagata 990-8560, Japan*

ARTICLE INFO

ABSTRACT

The J-PARC KOTO experiment aims to explore new physics beyond the Standard Model through the $K_L \to \pi^0 \nu \bar{\nu}$ decay. We installed a new photon-veto detector, named the Inner Barrel (IB), to improve the detection efficiency and the timing resolution for photons in the region transverse to the neutral beam. The IB is a 2.8-m-long cylindrical detector with a 1.5 m inner diameter. The IB is a lead-scintillator sampling shower counter with a 5-radiation-length thickness and with a low mass support structure, and fits inside the 14-radiation-length-thick cylindrical detector. Scintillating light is read out from both ends via wavelength shifting fibers with a short decay time. The design, construction and performance of the IB are presented in this paper.

1. Introduction

The rare kaon decay $K_L \to \pi^0 \nu \bar{\nu}$ is a sensitive probe to search for new physics beyond the Standard Model (SM). This direct CP-violating decay [1] is highly suppressed in the SM because it is a flavor-changing neutral current process. In the SM, the branching ratio is predicted to be 3×10^{-11} with small theoretical uncertainties of a few percent [2]. If the measured branching ratio is different from the SM prediction, it signifies the existence of new physics that breaks CP symmetry.

The first experiment dedicated to $K_L \to \pi^0 \nu \bar{\nu}$ was the E391a experiment at the KEK 12 GeV proton synchrotron, and it set an upper limit on the branching ratio to be 2.6×10^{-8} at the 90% confidence level [3]. A subsequent new experiment, named the KOTO (K0 at TOkai) experiment, was started at the Japan Proton Accelerator Research Complex (J-PARC) [4] with upgrades to achieve the sensitivity of 10^{-11} [5]. In the first major results from the data taken in 2015, the KOTO experiment improved the upper limit to 3.0×10^{-9} [6].

Fig. 1 shows a schematic cross-sectional view of the KOTO detector. The K_L beam collimated to a size of 8×8 cm^2 by the end of the 20-m-long beam line enters the decay region of the detector. There are two detector subsystems, which are located inside the vacuum chamber. One is the CsI calorimeter to detect two photons from the π^0 decay, and the other is a set of hermetic veto detectors to guarantee that there are no extra particles in the K_L decay. The Main Barrel (MB) detector [7], inherited from the E391a experiment, is a veto detector and has large coverage transverse to the neutral beam.

There are two requirements for the detector in the transverse region. One is better detection efficiency for photons to suppress backgrounds. The main background to $K_L \to \pi^0 \nu \bar{\nu}$ is the $K_L \to 2\pi^0$ decay in which two photons are detected in the CsI calorimeter and other two photons are undetected due to inefficiencies of the veto detectors. The other requirement is better timing resolution. A $K_L \to \pi^0 \nu \bar{\nu}$ decay event would be lost due to accidental hits in a veto detector under the high rate environment at J-PARC. If additional particles come within a close
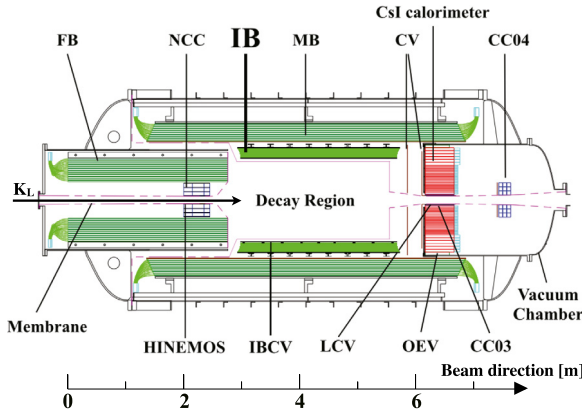
Fig. 1. Schematic cross-sectional side view of the KOTO detector. The beam enters from the left. The detector subsystems are placed in a 0.1 Pa vacuum region and are separated with membrane (solid-dashed line in Fig. 1) from the decay region in 5×10^{-5} Pa. Detectors placed downstream of the vacuum chamber are omitted in this figure. Inner Barrel (IB) is the new detector described in this paper. (For interpretation of the references to color in this figure legend, the reader is referred to the web version of this article.)

Fig. 2. Number of the $K_L \to 2\pi^0$ background events as a function of the photon detection threshold with (open circle) and without (triangle) the IB in the simulation. The corresponding number of SM events of the $K_L \to \pi^0\nu\bar{\nu}$ decay is 3.5.

timing to the K_L decay, the event would be vetoed by the extra hits in the KOTO detector. This is called accidental loss to the $K_L \to \pi^0\nu\bar{\nu}$ acceptance. A better timing resolution leads to a lower accidental loss.

Aiming to achieve the sensitivity of the KOTO experiment, we installed a new lead-scintillator sampling shower counter, named the Inner Barrel (IB), to the KOTO detector in 2016. By installing the additional high-performance IB detector inside the MB, we expect improvements in the timing resolution as well as the detection efficiency to the photons from the $K_L \to 2\pi^0$ background.

2. Design

2.1. Concept

The MB detector is a 5.5-m-long lead-scintillator sampling shower counter designed for the previous E391a experiment [7]. The thickness of the MB for normal incidence is 14 radiation lengths consisting of 15 inner layers (1 mm lead and 5 mm scintillator) and 30 outer layers (2 mm lead and 5 mm scintillator). For higher sensitivity measurement in the KOTO experiment, its detection efficiency can still be improved. There were three main reasons for the photon detection inefficiency in the MB. The first reason was punch-through, in which photons pass through material without interaction. This can be reduced by increasing the material thickness. The second reason was the sampling effect, in which the deposit energy in active parts fluctuates to below a detection threshold. The third reason was photo-nuclear interactions. To suppress the loss caused by the sampling fluctuation and due to photo-nuclear interactions, the portion of the non-active lead converter should be reduced. These are the motivations to develop and install the IB detector.

We evaluated the improvement by adding a new detector inside the MB based on the Monte Carlo simulation. The plots labeled with "MB only" in Fig. 2 show the estimated number of the $K_L \to 2\pi^0$ background events in the sensitivity of detecting 3.5 SM signal events without the IB detector. When the photon detection threshold is set at 1 MeV for the energy deposit in the scintillator layers (visible energy), 2.5 background events are expected. As the threshold is lowered, the background is reduced by recovering detection efficiency for photons with the energies of a-few-tens of MeV. This reduction, however, is limited as shown in the figure.

We decided to install the IB consisting of 1-mm-thick lead and 5-mm-thick plastic scintillator plates with the thickness of 5 radiation
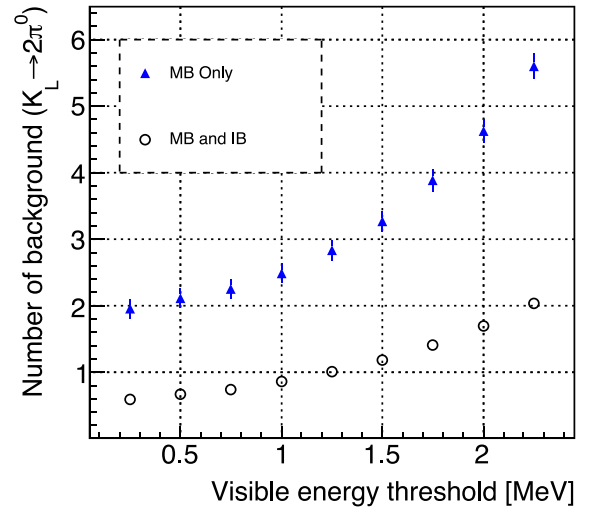
lengths inside the MB. The sampling ratio was the same as the 3-radiation-lengths inner layers of the MB. Increasing the total number of layers with higher sampling rate from 3 to 8 radiation lengths reduced the inefficiency due to the sampling fluctuation and photo-nuclear interactions. In making this decision, we considered (1) the acceptance reduction caused by narrowing the decay region in the detector, and (2) the limited space inside the vacuum chamber for the self-stand support structure and a path of readout fibers, which is explained later. The effect of the IB installation to the background rejection is shown as the plots labeled with "MB and IB" in Fig. 2; the number of the $K_L \to 2\pi^0$ background is expected to be suppressed by a factor three.[4]

From the background estimation in Fig. 2, we set an IB's visible energy threshold to be 0.5 MeV. To avoid thermal-electron noise, the corresponding threshold to the detected number of photoelectrons (p.e.) should be larger than 2 p.e. Thus, we required the light yield should not be smaller than 5 p.e./MeV anywhere in the IB detector.

To achieve a better timing resolution, scintillation materials with short decay times were adopted based on the investigation of materials. The timing resolution in the MB is dominated by the decay time of the wavelength shifting (WLS) fibers. For the IB, we adopted new fibers which had 3 times shorter decay time and comparable light yield, compared to those used in the MB.

2.2. Structure

Fig. 3 shows the design of the structure. The IB consists of the top and bottom modules, and other 30 modules with the same trapezoidal shape. The modules consist of 25 layers of 5-mm-thick scintillator plates (G-tech GT-MS155) and 24 layers of 1-mm-thick lead plates, corresponding to the thickness of $5X_0$ in total. To prevent the module from bending, a 3-mm-thick stainless steel plate and a 10-mm-thick aluminum plate are placed on the inner side and outer side of modules, respectively. The stainless steel plate acts as the first layer of the converter. The module is secured at 9 points with 3/4"-wide and 0.76-mm-thick stainless steel bands. The trapezoidal modules are oriented as shown in Fig. 3 to apply tension on the stainless steel bands by the module's own weight.

As shown in Fig. 4, each scintillator plate is sandwiched between two 0.19-mm-thick reflector sheets (TiO$_2$ PET, Toray RW188 E60L).

---

[4] Two thirds of the background reduction was brought from the detector thickness to reduce punch-through.
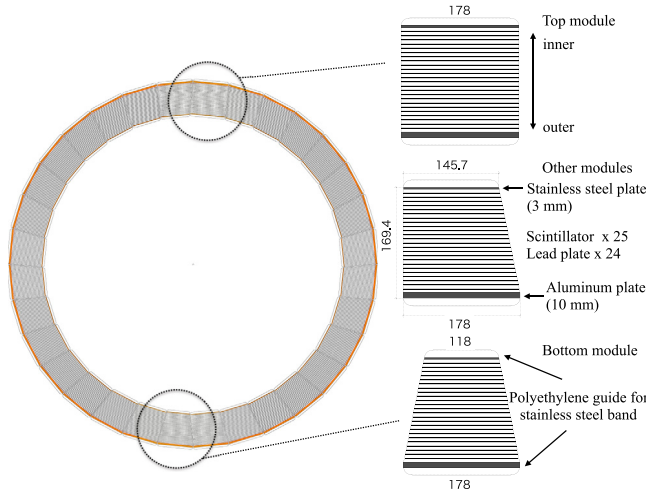
Fig. 3. Schematic view of each IB module. It consists of a stainless steel plate, 25 layers of scintillator plates and 24 layers of lead plates, and an aluminum plate.
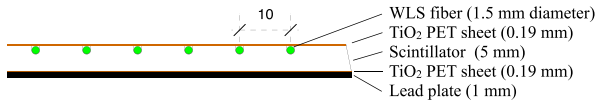

Fig. 4. Schematic view of one layer of the module. Each scintillator plate is sandwiched by TiO_2 PET sheets. The 1.5-mm diameter WLS fibers are implanted in scintillator plates with 10 mm intervals. The groove is 1.7 mm wide (0.2 mm larger than the fiber diameter) and 1.7 mm deep, and has an U-shaped cross-section not to leave bubbles at the edge at the bottom.

The single-clad WLS fibers, Saint-Gobain BCF-92, are implanted in the scintillator plate and glued with UV-cure adhesive (NORLAND Products Inc. NOA61).[5] We chose this fiber due to the better timing resolution because the decay constant of BCF-92, 2.7 ns, was shorter than that for Kuraray Y-11 used for the MB (8.8 ns). We decided to use the 1.5-mm-diameter fibers for the IB to obtain a higher light yield compared to 1-mm fibers used for the MB.[6]

The 32 modules are assembled to form a cylinder as shown in Fig. 5. The cylinder is 2.8 m long, and has a 1.5 m (1.9 m) inner (outer) diameter. The total weight of the modules is 6 tons. To support the modules with the minimal amount of material, we employed eight rings with I-shaped cross-section. The rings were made by machining forged aluminum alloy (AL-7075-T7352) rings to have a circular shape outside and a regular 32-sided polygon shape inside. The tolerance for the outer diameter and inner "diameter" were ±0.25 mm, and other typical tolerances were ±0.13 mm. The reason for using aluminum alloy is that the number of background events was expected to be reduced for lower amount of the dead material in terms of the radiation length. This effect is shown in the background estimation shown in Fig. 6.

To detect charged particles from K_L decays and to work as the first layer of the sampling detector, charged veto counters (IBCVs) are attached to the inner surface of the IB. The IBCVs are 5-mm-thick scintillator plates with WLS fibers glued with BC-600, similar to the scintillator layers of the IB.

---

[5] The scintillator plates for the top and bottom modules and 3% of all the other scintillator plates are glued with two-part adhesive (Saint-Gobain BC-600) due to a trouble that will be described in Section 3.3.

[6] In the measurement with double-clad fibers, the 1.5-mm fibers resulted in a 1.7 times better light yield compared to the 1-mm fibers.
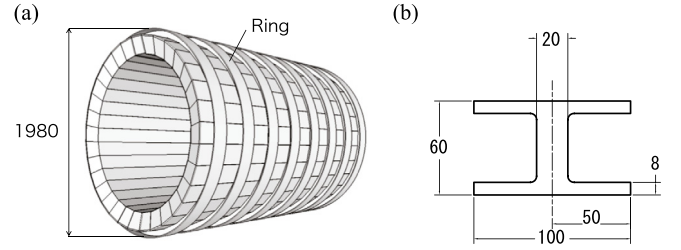

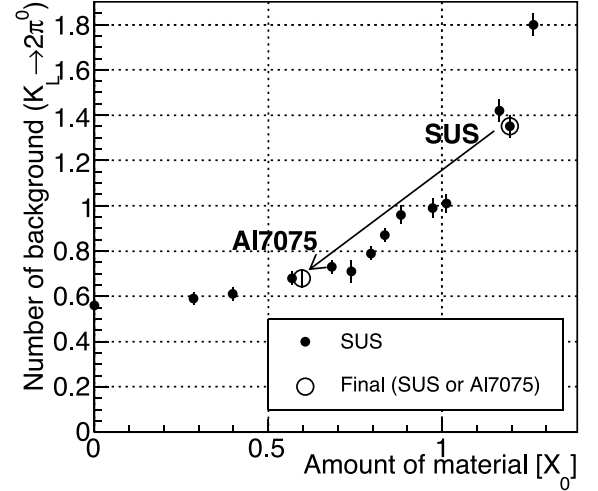**Fig. 5.** (a) Inner Barrel supported by 8 rings; (b) cross-section of the rings.

Fig. 6. Number of the $K_L \to 2\pi^0$ background events as a function of the areal density of the Inner Barrel support structure, where 3.5 SM signal events are expected. Closed circles show the various designs made of stainless steel (SUS). Open circles show needed material amount to support the IB in case of stainless steel (SUS) and Al-alloy (Al7075). The amount of material plotted in the horizontal axis, in the unit of radiation length (X_0), is averaged over the area of the Inner Barrel's total outside surface.

2.3. Readout

The light from the WLS fibers is read out with a photomultiplier tube (PMT) at each end (Hamamatsu R329-EGP [8] for upstream, and Hamamatsu R7724-100 for downstream[7]) of each module. A 5-mm-thick cured elastomer (Momentive Performance Materials Inc. TSE3032) is used to optically connect the WLS fibers and the PMTs. As shown in Fig. 7, the PMT bases for the IB are placed at 2 m away from the PMTs in order to fix the bases to the water cooling pipe for heat removal in vacuum at 0.1 Pa. The individual dynodes of the PMTs and the bases are connected with 2-m-long HV lines (UL3725). For the last three dynodes, we added capacitors and resistors to suppress the voltage drop which distorts the waveforms.

For the IBCV readout, we employed Hamamatsu R329 PMTs placed near the water cooling pipe. Instead of connecting the WLS fibers of the IBCV directly to the PMTs, we optically connected a 2 m long Polymer Light Guide (PLG) [9], which was a soft acrylic resin tube with a diameter of 14 mm, between the WLS fibers and the PMTs. This method is more resistant to the damage when passing it through a narrow gap and is more cost-effective than the direct connection. In a test, we confirmed that the light loss due to the PLG connection was approximately 1%.

For both the IB and IBCV, signals from PMTs are digitized by ADCs in the KOTO data acquisition system. Although the MB is read out with 125 MHz ADCs with Bessel filter to widen the pulses [10,11], the IB and

---

[7] The R7724-100 PMTs were used due to the production stop of R329-EGP PMT.
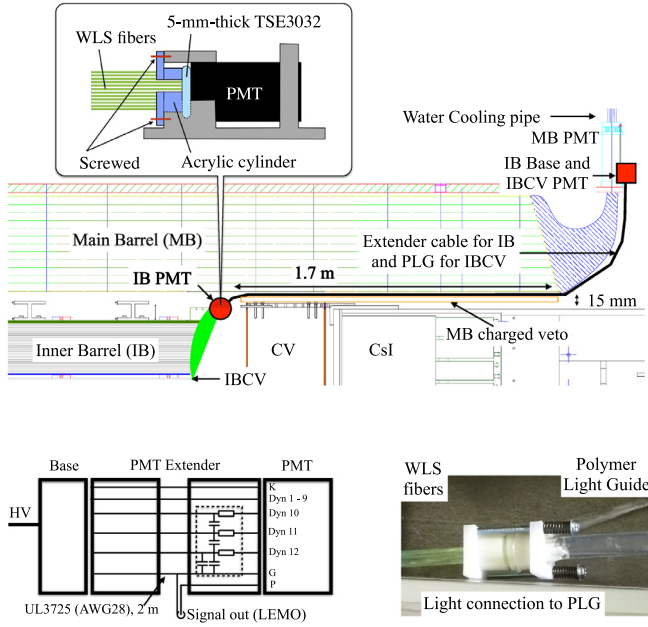
Fig. 7. Enlarged view of Fig. 1 at around the downstream PMT location. Bottom two figures are a schematic drawing of a PMT and its base for the IB modules (left) and a photograph of the PLG connection for the IBCVs (right).
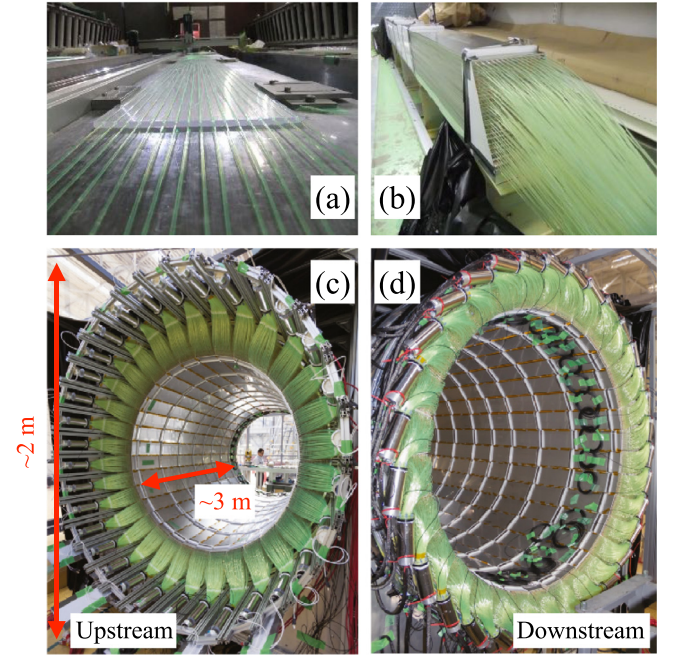

Fig. 8. Photographs of (a) scintillator plate with WLS fibers; (b) one module; assembled IB detector viewed from the (c) upstream and (d) downstream.
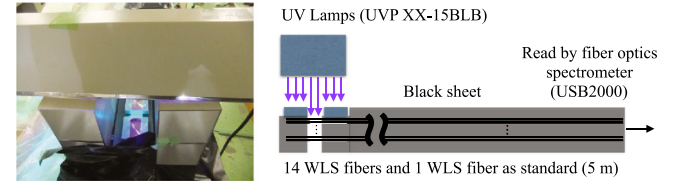

Fig. 9. Photograph (left) and schematic view (right) of the light yield measurement with a spectrometer. A standard fiber was always measured as a reference.

IBCV are read out with 500 MHz ADCs without the Bessel filter [12]. This new readout would improve the timing resolution by a factor 2 based on the waveform simulation with decay-time parameters of the BCF-92 fibers.

3. Fabrication

For the detector fabrication, firstly we prepared scintillator plates with WLS fibers, secondly stacked the scintillator plates and lead sheets to form modules, and finally assembled the modules together to form the detector. Fig. 8 shows the modules at each production step.

3.1. Scintillator

The 3.0-m-long and 40-cm-wide scintillators were produced by an extrusion-mold process. The GT-MS155 scintillators are composed of MS-resin (80% polystyrene and 20% meta-acrylate) mixed with 1.2% para-terphenyl and 0.045% POPOP as luminant. Although the extrusion method is able to control the thickness much better than the cast method, the thickness of the center in the direction of width was less than the edges by 3% (0.15 mm). We cut the scintillators into two pieces to the width designed for each layer (118∼178 mm) and stacked them with the thinner and thicker sides alternately to control the thickness of the module.

The scintillators were grooved to attach the WLS fibers with a 10 mm pitch multiple-blade saw. The straightness of the scintillators and the grooves was kept to be less than 0.5 mm.

3.2. Fiber attachment

We cut the fibers into 5 m lengths. To check for fiber damage, we measured the light intensity at the far end of the fiber with a spectrometer (USB2000, Ocean Optics Inc.) by illuminating the other end with UV light (365 nm) for all the fibers as shown in Fig. 9. Based on the results of the measurement with an accuracy of 15%, we rejected 0.1% of all the fibers. Because the light-intensity variation was 17% (RMS) among the production reels, we alternatively placed fibers in

the grooves from a pair of reels with low and high light yields in order to make the light yield uniform among modules.

We filled the adhesive NOA61 in the scintillator grooves with a dispenser on automatic moving stages. We then cured the adhesive by shining UV light with a light flux of 2 mW/cm^2 for 50 min under the tension of 0.4 kg on each fiber. The accumulated light energy was 6 J/cm^2.

3.3. Treatment after fiber attachment

After the fibers were glued some cracks appeared in the scintillators caused by uncured adhesive. For the scintillators with large cracks, we made new scintillators with fibers glued with BC-600 optical cement. Other scintillators with no serious cracks were annealed at 80 °C for 3 h to increase the chemical stability of the scintillator plates.

After the annealing, the scintillator plates were placed in vacuum (pre-evacuation) for 3 days. This process was needed to suppress the outgassing rate in the vacuum vessel of the KOTO detector system after the IB installation. The main sources of outgassing were uncured adhesive and moisture absorbed in the scintillator. According to an evacuation test,[8] the outgassing rate from all the IB modules was reduced from 0.4 Pa m^3/s to 0.04 Pa m^3/s. This rate was comparable with the amount of the outgas from all the other KOTO detectors staying for long time in vacuum.

---

[8] At the evacuation test, we tested 25 scintillators for three days. 0.4 Pa m^3/s is scaled to the all scintillators for the 32 IB modules.

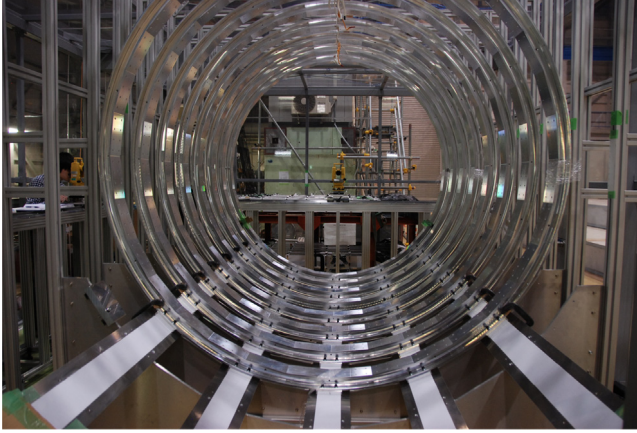**Fig. 10.** (a) Photograph of bundling the module with stainless steel bands; (b) cut and polished fiber bundle.

Fig. 11. Photograph of eight Al-alloy rings placed on Teflon rails and aligned to ±0.1 mm with sliding theodolites.

3.4. Module production

As shown in Fig. 10, we stacked the module components, and bundled the module with the stainless steel bands while compressing them with 4.5 tons of force. The module dimensions met the design within ±1 mm after releasing the pressure. We glued the bundle of fibers in a plastic jig with epoxy resin (CY-230 resin and HY-951 hardener), and cut and polished the cross-section.

3.5. Assembling

An aluminum frame structure with five aluminum rails with Teflon sheets (Teflon rails) shown in Fig. 11 was used to support the IB detector during the assembling and inserting the IB detector inside the MB. The eight Al-alloy rings with aluminum pads were placed on the rails. Teflon sheets were glued on the surfaces of the pads and the rails with ALTECO PR960 primer and "88" instant glue [13]. With the low coefficient of static friction between the Teflon sheets, 0.04∼0.05, the 6-ton detector was able to slide on the rails.

We mounted the assembled modules from the bottom on the inside of eight Al-alloy rings. The top module with a rectangular cross-section was slid into the position at the end.

3.6. Installation

Fig. 12 shows the IB just before inserting it to the MB in the experimental area of KOTO. To insert the IB into the MB, additional Teflon rails were installed on the inner surface of the MB, and in the gap between the MB and the aluminum frame. The IB was pulled into the MB with chain-blocks and was fixed. After the insertion, the IBCV counters were installed and the MB charged veto counters were installed on the downstream part of the MB as shown in Fig. 7.

Fig. 12. Photograph of the IB (forward) just before its insertion to the MB (backward).

4. Performance

The following measurements of the IB were made at each step of the production, and before and after the installation.

4.1. Light yield

In this section, we discuss the position dependence of the light yield of two items: a single WLS fiber and a typical IB module. The light yield Y was parametrized as:

$$Y(d) = A_1 \exp\left(\frac{-d}{L_1}\right) + A_2 \exp\left(\frac{-d}{L_2}\right), \tag{1}$$

where A_1 and A_2 are normalization factors, L_1 and L_2 are shorter and longer components of the attenuation lengths, respectively, and d is the distance from the PMT surface.

The light yield measurement for the single WLS fiber was performed with a similar setup to Fig. 9. In this case, we connected a PMT at the end of a 7-m-long fiber and illuminated the fiber with a blue LED (405 nm) at the 50 cm intervals. The light yield was estimated from the pulse height distributions of the output signals. The result is plotted in Fig. 13(a), where the light yield was normalized to the value at $d = 530$ cm. Two components of the attenuation lengths were $L_1 = (67.0 \pm 5.4)$ cm and $L_2 = (418.6 \pm 13.0)$ cm (see the fitted curve in the figure).

To evaluate the performance of the fabricated module, we measured the light yield with cosmic rays passing through the 8 points along the longitudinal direction of the module shown in Fig. 14. The hit positions of the cosmic rays were defined with the top and bottom pairs of the trigger counters. We connected a PMT R329-EGP (PMT1) at the upstream end of the WLS fibers; the same model of the PMT (PMT2) was attached to the downstream side via 2-m-long PLG. Fig. 13(b) shows the position dependence of the light yield for the fabricated module. The attenuation lengths were $L_1 = (59.9 \pm 25.2)$ cm and $L_2 = (389.9 \pm 13.4)$ cm, evaluated at >90 cm from the PMTs. Because the minimum distance between the PMTs and the edge of the module is 90 cm, the light attenuation in the module is dominated by the L_2 component. The L_2 for the module is consistent with the L_2 of the WLS fibers.

The absolute light yield of all the modules were examined with cosmic-rays before mounting them on the rings. The setup of the measurement was slightly different from that shown in Fig. 14. In order to make the setup similar to the KOTO detector, the PLG and the R329-EGP PMT were removed and R7724 PMT was connected. A single pair of the trigger counters was placed at the center of each module; thus,
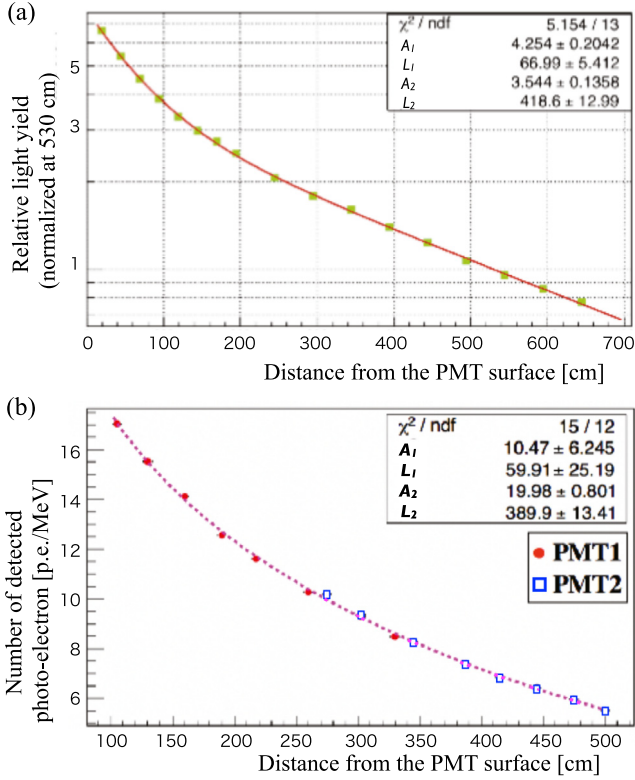
(a)

(b)

χ² / ndf	5.154 / 13
A_1	4.254 ± 0.2042
L_1	66.99 ± 5.412
A_2	3.544 ± 0.1358
L_2	418.6 ± 12.99

χ² / ndf	15 / 12
A_1	10.47 ± 6.245
L_1	59.91± 25.19
A_2	19.98 ± 0.801
L_2	389.9 ± 13.41

Fig. 13. Light yield as a function of the distance from a PMT measured with LED for a BCF92 fiber (a) and with cosmic-rays for a module (b). PMT1 and PMT2 in the bottom figure are the ones shown in Fig. 14.
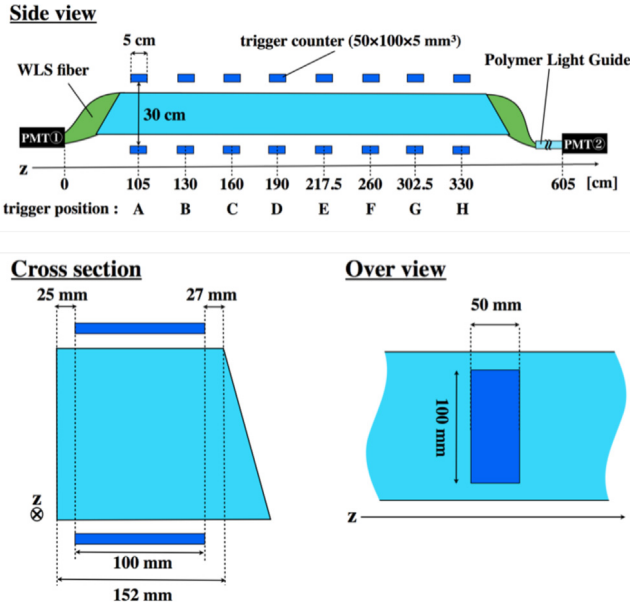

Fig. 14. Setup for the studies with cosmic-rays for a module. PMT1 and PMT2 are R329-EGP PMTs. The trigger counters defined the timing of hits.

we measured the light yield at the center in this case. To evaluate on the safety side, the light yield at the center was scaled to that measured at the far end of the module by correcting with the attenuation lengths shown in Fig. 13(b). The results for all the modules are plotted in Fig. 15. The average of the light yields at the farthest ends of all the modules were 6.5 p.e./MeV for upstream PMTs and 5.3 p.e./MeV for
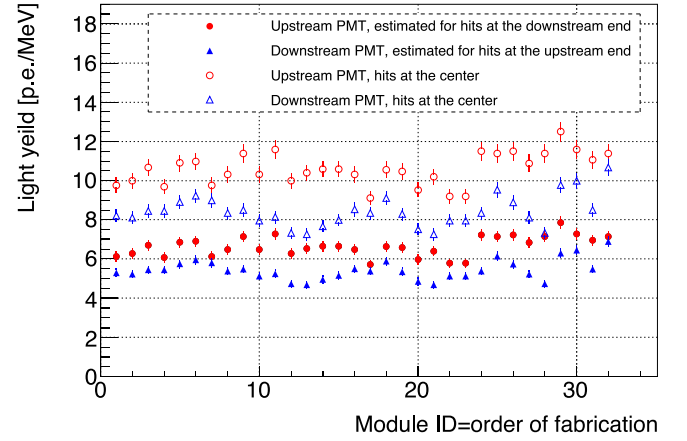

Fig. 15. Measured light yield for hits at the center of the module (open circles and triangles), and the light yield for hits at the farther end from the PMT estimated based on the measurement and the attenuation length (closed circles and triangles).

downstream PMTs.[9] This meets the requirement of the light yield for the IB detector (> 5 p.e./MeV).

4.2. Timing resolution

The timing resolution was measured at 8 locations of the typical module with the same setup shown in Fig. 14. We estimated the resolution from the spread of the time-difference distribution of the PMT1 and PMT2.[10] The result is shown in Fig. 16 as a function of the number of photoelectrons $N_{p.e.}$ derived from the measured values of Fig. 13(b) and the energy deposited by cosmic rays passing through the module (25 MeV). As shown in the fitted curve in Fig. 16, the timing resolution is represented as $(4.85 \pm 0.03)/\sqrt{N_{p.e.}}$ [ns/(p.e.)$^{1/2}$] in the range of $N_{p.e.} = 100 \sim 500$.

After the IB was installed inside the MB, we compared the hit timings between the IB and MB modules with cosmic-rays. Each MB module was read out with two PMTs for the inner and outer layers. The obtained timing resolution was (0.22±0.02) ns for the 25 MeV deposit in the plastic scintillator in the IB, (0.41 ± 0.01) ns for the 15 MeV deposit in the MB inner layers, and (0.31 ± 0.02) ns for the 30 MeV deposit in the MB outer layers. We achieved a better timing resolution for the IB than for the MB inner and outer layers. The result signifies 30% better timing resolution for the IB than for the MB to the same energy deposit.

To evaluate the timing resolution to the lower energy deposits ($N_{p.e.} < 100$), we simulated the waveforms for various numbers of observed photoelectrons by summing up the measured 1 p.e. pulses using an appropriate timing probability density function (PDF). For this purpose, a large number of cosmic-ray signal waveforms and 1 p.e. signal waveforms from the PMT were recorded in advance with a 500-MHz-sampling oscilloscope to obtain the averaged waveform. Fig. 17 shows (a) a typical cosmic-ray signal and (b) the averaged waveform. The following empirical timing PDF with an asymmetric Gaussian distribution [14] was assumed:

$$f(t) = A \exp\left[-\frac{(t-\mu)^2}{2\left(a(t-\mu)+\sigma\right)^2}\right], \qquad (2)$$

[9] The difference of the light yield between upstream and downstream was explained as the difference of quantum efficiency of the PMTs in the upstream (~20%) and in the downstream (~15%) at the peak emission wavelength of the fiber (492 nm).

[10] The timing spreads from the trigger counters themselves, 0.37 ns, and from the allowed range of the hit positions of the cosmic rays to the z direction, 0.07 ns, were subtracted quadratically. The latter, due to the finite size of the trigger counters (50 mm as shown in Fig. 14), was corrected for based on the estimation of the position distribution for the triggered cosmic-rays with the Monte Carlo estimation.
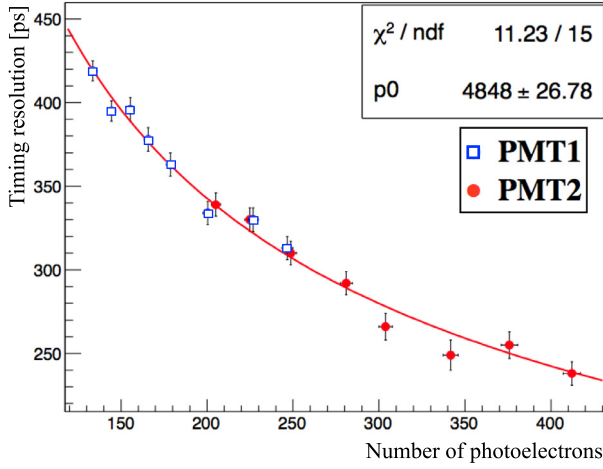
Fig. 16. Timing resolution as a function of the number of photoelectrons. The error bars for each point in the x-axis shows the systematic uncertainty of the position to set the trigger counters. The red curve shows the fitting function $f = p_0/\sqrt{N_{\text{p.e.}}}$, where $N_{\text{p.e.}}$ is the number of photoelectrons; $N_{\text{p.e.}}$ is deducted from the light yield measured at each distance from a PMT. The PMT1 and PMT2 are the ones shown in Fig. 14.
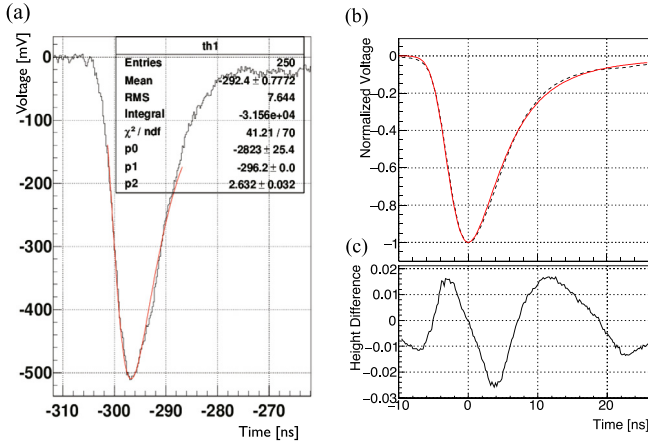

Fig. 18. Hit position dependence of the timing resolution estimated with waveform simulation. The position at 0 mm means the upstream edge of the detector. Closed (open) circles show the 10 p.e. (12 p.e.) readout from the upstream R329-EGP PMT, and closed (open) triangles show 10 p.e. (12 p.e.) readout from the downstream R7724 PMT.

Fig. 17. (a) Waveform of a cosmic-ray event fitted by the Landau distribution to define the pulse peak; (b) averaged waveform of the cosmic-ray signals (dashed curve) and the reconstructed waveform with photoelectrons distributed according to the timing PDF (solid curve); (c) height difference between these two waveforms.

where t is time, σ denotes the width of waveform, and a is an asymmetric parameter; A and μ are the peak height and peak timing, respectively. The parameters a and σ are characterized by the light emission process of the scintillator, the light absorption and emission processes, and the transmittance of the WLS fibers. In order to determine these two parameters, we generated a waveform from the averaged 1 p.e. pulses distributed with the timing PDF and fitted this waveform to the averaged waveform of the cosmic-ray signals by using a χ^2 minimization algorithm. As shown in Fig. 17(b), the reconstructed waveform reproduced the typical waveform for the cosmic rays with $a = 0.20$–0.25 and $\sigma = 3.4$–4.0 ns, where the discrepancy was within 3% for all the parts in the waveform (see Fig. 17(c)). In this way, these parameters were determined at four positions in the longitudinal direction (325 mm, 1275 mm, 1552 mm, and 2402 mm from the upstream edge of the detector) and were used to evaluate the timing resolution in the low energy region.

Fig. 18 shows the position dependence of the timing resolution for low energy deposits based on the timing PDF method. The noise fluctuation observed at the KOTO experimental area was included in the generated waveforms. The 12 p.e. (10 p.e.) means the 1.8 MeV energy deposit for far end readout of upstream (downstream) PMTs. For the
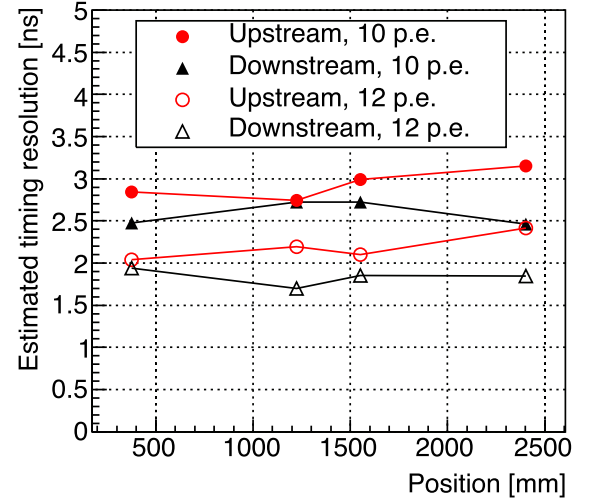
same PMTs, the timing resolution for 12 p.e. was 30% better than that for 10 p.e. because the effect of electric noise is less dominant. In both the 10 p.e. and 12 p.e. cases, there were 10%–20% position dependence on the timing resolution, which arose from the waveform broadening due to the long readout distance. The reason for the small systematic difference for the same number of photoelectrons between the upstream and downstream readouts was unclear but presumably due to the difference of models of the PMTs. This systematical difference partially canceled the difference caused by the photoelectron statistics. In total, the timing resolution near the visible energy threshold had a 20% difference at most between the upstream and downstream readouts for the same energy deposits.

4.3. Calibration

After the IB was installed to the KOTO detector, the measured energy and timing were calibrated with cosmic-rays. The hit position along the beam direction was determined with the timing difference of two PMTs at the upstream and downstream ends as shown in Fig. 19. The timing difference shows a flat plateau distribution, which means the propagation velocity should be constant in the module. The module length was defined with the step functions with Gaussian tails. The mean of the propagation velocities for all the modules was (179.0 ± 0.1) mm/ns. The value agreed with the result in the module test, (179.4 ± 1.7) mm/ns, measured before the installation.

For the energy calibration, we fitted the light yield for the tracks of minimum ionizing particle (MIP) based on the empirical function of the MB [7]. The light yield Q_u (Q_d) read out from the upstream (downstream) readout was fitted as a function of the z-position as:

$$Q_u(z) = C_u \Delta E \exp \frac{-z}{\lambda_u + \alpha_u z}, \qquad (3)$$

and

$$Q_d(z) = C_d \Delta E \exp \frac{z}{\lambda_d - \alpha_d z}, \qquad (4)$$

where C_u (C_d) is the calibration constant in units of ADC count per MeV for the upstream (downstream) readout, ΔE is the fixed value of the deposit energy 25 MeV of the cosmic-ray MIP tracks, and the effective attenuation length is made dependent on the hit position z, centered around λ_u (λ_d) in units of mm with a non-dimensional factor α_u (α_d). Fig. 20 shows the measured ADC counts and the parameters obtained by the fitting. The energy scales of all the channels were tuned to an accuracy of a few percents of fitting error.
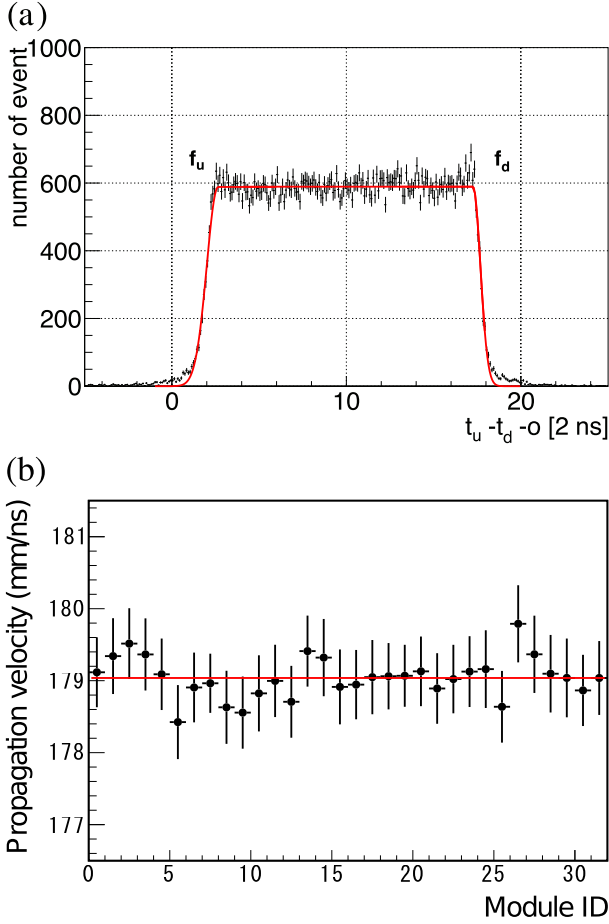
(a)

(b)

Fig. 19. (a) Timing difference between the upstream and downstream readouts ($t_u - t_d - o$) for a module in units of sampling frequency of ADCs (2 ns), where o is the offset in the data acquisition. Two curves f_u and f_d show the step functions with Gaussian tails. (b) Propagation velocity for all the modules.

(a)

(b)

Fig. 20. (a) Position dependences of the readout ADC counts of the IB module measured for energy calibration, and fitting results to the empirical functions. The position at 0 mm means the center of the detector on the beam axis. (b) Fitting results of the empirical functions for all the modules. The upstream and downstream readouts for ith module are shown in the values at PMT ID = i and $i+32$ ($i = 0 \sim 31$), respectively.

5. Conclusion

We installed a new cylindrical photon-veto detector, IB, to the KOTO detector in 2016 in order to suppress the main background $K_L \rightarrow 2\pi^0$ to the $K_L \rightarrow \pi^0 \nu \bar{\nu}$ decay by a factor 3. The requirement of the light yield, ≥ 5 p.e., and the 30% better timing resolution than that of the MB were evaluated and confirmed with the cosmic ray data. The technique for the energy and timing calibrations with cosmic-rays was also established.

Declaration of competing interest

The authors declare that they have no known competing financial interests or personal relationships that could have appeared to influence the work reported in this paper.

CRediT authorship contribution statement

R. Murayama: Methodology, Validation, Writing - original draft. **M. Togawa:** Methodology, Validation, Writing - original draft. **J.K. Ahn:** Supervision. **J. Comfort:** Validation, Funding acquisition. **T. Inagaki:** Methodology, Writing - review & editing. **M. Isoe:** Investigation. **I. Kamiji:** Investigation. **E.J. Kim:** Supervision, Funding acquisition. **J.L. Kim:** Formal analysis. **T.K. Komatsubara:** Writing - review & editing, Resources. **G.Y. Lim:** Conceptualization, Supervision. **T. Matsumura:** Writing - review & editing. **K. Miyazaki:** Validation, Investigation. **H. Nanjo:** Software. **T. Nomura:** Resources. **H. Okuno:**
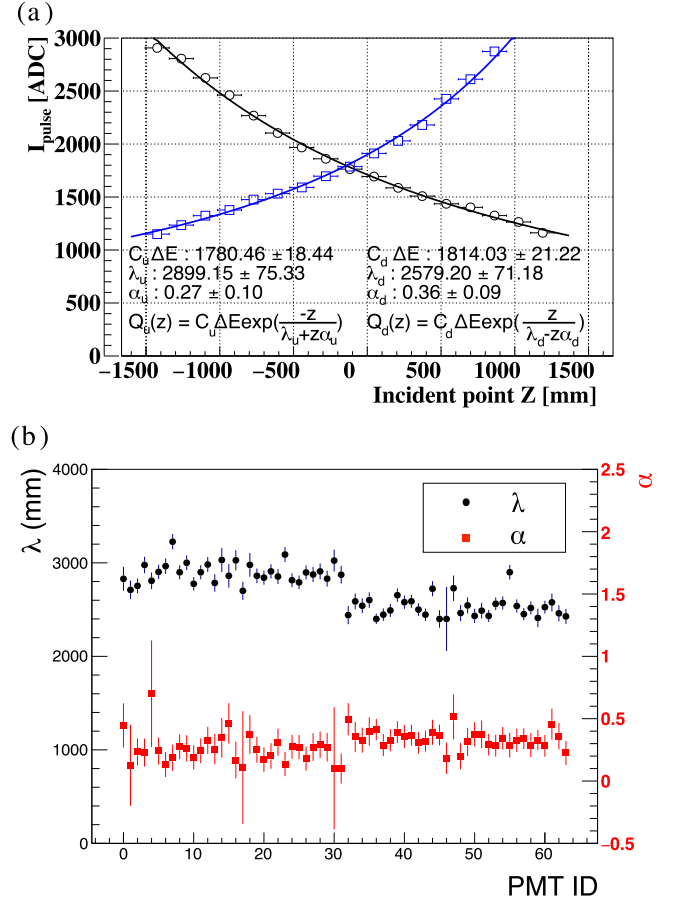
Methodology. **E. Pod:** Investigation, Methodology. **T. Sato:** Methodology. **K. Shiomi:** Methodology. **Y. Tajima:** Resources. **T. Toyoda:** Validation, Investigation. **Y.W. Wah:** Project administration, Funding acquisition. **H. Watanabe:** Resources. **T. Yamanaka:** Project administration, Funding acquisition, Investigation, Methodology.

Acknowledgments

References

[1] L.S. Littenberg, Phys. Rev. D 39 (1989) 3322.
[2] A.J. Buras, D. Buttazzo, J. Girrbach-Noe, R. Knegjens, J. High Energy Phys. 11 (2015) 033.
[3] J.K. Ahn, et al., Phys. Rev. D 81 (2010) 072004.

[4] S. Nagamiya, Prog. Theor. Exp. Phys. 2012 (2012) 02B001.
[5] J. Comfort, et al., J-PARC E14 Collaboration, Proposal for $K_L^0 \rightarrow \pi^0 \nu \bar{\nu}$ Experiment at J-PARC (https://j-parc.jp/researcher/Hadon/en/pac_0606/pdf/p14-Yamanaka.pdf).
[6] J.K. Ahn, et al., Phys. Rev. Lett. 122 (2019) 021802.
[7] Y. Tajima, et al., Nucl. Instrum. Methods A 592 (2008) 261.
[8] M. Itaya, et al., Nucl. Instrum. Methods A 522 (2004) 477.
[9] http://www.fiberopticlight.com.
[10] Y. Sugiyama, et al., IEEE Trans. Nucl. Sci. 62 (2015) 1125.
[11] M. Bogdan, J. Genat, Y. Wah, 2009 16th IEEE-NPSS Real Time Conference, 2009.
[12] M. Bogdan, J. Genat, Y. Wah, 2010 17th IEEE-NPSS Real Time Conference, 2010.
[13] http://www.alteco.co.jp/en/.
[14] E. Iwai, et al., Nucl. Instrum. Methods A 786 (2015) 135.